

Propagation of light in metallic nanowire arrays: Finite-difference time-domain studies of silver cylinders

Stephen K. Gray* and Teobald Kupka

Chemistry Division, Argonne National Laboratory, Argonne, Illinois 60439, USA

(Received 6 January 2003; published 16 July 2003)

Finite-difference time-domain studies of a variety of silver cylinder arrays with nanometer-scale diameters (nanowires) interacting with light are presented. We show how reasonable estimates of scattering and absorption cross sections for metallic nanoscale objects can be obtained from such calculations. We then study the explicit time-domain behavior of both simple linear chains of such cylinders, as well as more elaborate arrays. A funnel-like configuration is found to be one interesting possibility for achieving propagation of light through features confined in one dimension to less than 100 nm.

DOI: 10.1103/PhysRevB.68.045415

PACS number(s): 78.67.-n, 42.25.Fx, 42.79.Gn, 73.20.Mf

I. INTRODUCTION

The absorption and scattering of light by small particles, including metal nanoparticles (MNP's), is an old and extensively studied subject.¹ Nonetheless modern experimental methods, including near-field scanning optical microscopy² (NSOM) and nanolithography,³ coupled with the desire to develop nanophotonics and nanoelectronics applications, have brought this venerable area to the forefront of current scientific research.

Here we show how finite-difference time-domain⁴⁻⁶ FDTD calculations can be used to study light interacting with arrays of silver cylinders with nanoscale diameters, and we carry out a variety of studies of various configurations. The cylinders can be viewed as metallic nanowires and exhibit optical behavior similar to MNP's. In particular, surface plasmon polaritons (SPP's), resonance interactions of light with electronic charge density near the metal surface,⁷ can play an important role. Motivation for our work comes from earlier theoretical work suggesting that coupled SPP's in arrays of MNP's could be used to confine and guide light at the subdiffraction limit.⁸⁻¹⁰ In a related development, SPP-mediated subdiffraction limit transport of light in gold nanowires has recently been demonstrated.¹¹ Additional motivation for our work is provided by recent work of Wurtz and co-workers using NSOM techniques to explore a variety of aspects of silver nanoparticles,¹²⁻¹⁴ as well as ultrafast spectroscopic work of Scherer and co-workers.^{15,16}

Since Quinten *et al.*⁸ suggested the possibility of propagating light in chains of MNP's, a number of other theoretical studies have appeared. Most of this work is based on frequency-domain solutions to Maxwell's equations. The interesting theoretical studies of Kottmann, Martin, and co-workers¹⁷⁻¹⁹ and Stockman, Faleev, and Bergman^{20,21} are particularly relevant to our work. Actually, the electrodynamics of MNP's and nanoparticle clusters has also been of interest in physical chemistry for some time now, owing to the phenomenon of surface-enhanced Raman spectroscopy (SERS).²² Kelly and co-workers have carried out a variety of theoretical studies of MNP clusters²³⁻²⁷ of relevance to SERS and also to biosensors. The theoretical approach adopted here, a time-domain one, is complementary to the

work noted above. It is also very general and can be adapted to a variety of problems. See also the important related work of Maier, Kik, and Atwater,¹⁰ who recently presented FDTD results pertaining to a collective surface-plasmon resonance in linear arrays of gold spheres.

Section II outlines our theoretical and computational methods. Section III presents cross-section results for linear chains, and Sec. IV presents time-evolution studies of various cylinder arrays. A funnel-like configuration is shown to have some promise for achieving propagation of light through sub-100 nm features. Section V concludes the paper and the Appendix discusses our modeling of the dielectric constant.

II. THEORETICAL METHODS

The systems of interest to us are lossy and dispersive, so that special care must be taken in designing an appropriate FDTD (Refs. 4-6) approach. We outline here the approach we have found to be useful.

A. FDTD scheme in the presence of metal nanoparticles

Frequency-domain solutions to Maxwell's equations for light interacting with materials are constructed by allowing spatial (x, y, z) and possibly light frequency (ω) variation in the dielectric constant ϵ . In a region of space $\{x, y, z\}$ occupied by a metal, ϵ can be complex valued and frequency dependent: $\epsilon = \epsilon_o[\epsilon_r(\omega) + i\epsilon_i(\omega)]$. A positive imaginary part ϵ_i is associated with absorption and a negative real part ϵ_r with reflection. Difficulties arise in attempting to construct time-domain solutions to Maxwell's equations via the FDTD method in this case. The inclusion of frequency dependence (dispersion) in ϵ is one issue. A more pragmatic problem is that negative ϵ_r values make the standard time iteration scheme unstable. One alternative is to introduce current-density terms into Maxwell's equation that are formally equivalent (upon Fourier transformation to the frequency domain) to the use of a complex-valued, frequency-dependent dielectric constant.^{5,28-31} For example, we adopt the following limiting case for Maxwell's equations,

$$\frac{\partial}{\partial t} \mathbf{E}(x, y, z, t) = \frac{1}{\epsilon_{\text{eff}}(x, y, z)} [\nabla \times \mathbf{H}(x, y, z, t) - \mathbf{J}(x, y, z, t)],$$

$$\frac{\partial}{\partial t} \mathbf{H}(x, y, z, t) = -\frac{1}{\mu_o} \nabla \times \mathbf{E}(x, y, z, t),$$

$$\frac{\partial}{\partial t} \mathbf{J}(x, y, z, t) = \alpha(x, y, z) \mathbf{J}(x, y, z, t) + \beta(x, y, z) \mathbf{E}(x, y, z, t). \quad (2.1)$$

In regions of free space, or some dielectric material with a positive, real dielectric constant, $\alpha = \beta = 0$, and if the current-density vector \mathbf{J} is initially zero in these regions, it remains zero. In free space, $\epsilon_{\text{eff}} = \epsilon_o$. In metallic regions, ϵ_{eff} , α , and β take on values characteristic of the metal. Equation (2.1) is consistent with the real and imaginary parts of a standard Drude model¹ for the dielectric constant of a metal. However, as outlined in the Appendix, we can numerically fit a Drude model to empirical dielectric constant behavior in any localized region of frequency space, achieving a reasonably accurate modeling of any frequency region. (See Refs. 5, 28, and 29 for other approaches.) The three parameters of the Drude model (see the Appendix) are $\epsilon_r(\infty)$, ω_D , and Γ_D . In a metallic region we then use

$$\begin{aligned} \epsilon_{\text{eff}} &= \epsilon_o \epsilon_r(\infty), \\ \alpha &= -\Gamma_D, \\ \beta &= \epsilon_o \omega_D^2 \end{aligned} \quad (2.2)$$

in Eq. (2.1).

Specializing to the transverse electric (TE) case with cylindrical symmetry, we drop the z coordinate in all equations and deal with just three of the six field components, E_x , E_y , and H_z ($E_z = H_x = H_y = 0$). With discrete time steps τ , and notation $E_x^{n+1/2}(x, y) \equiv E_x[x, y, t = (n+1/2)\tau]$, etc., for $n = 0, 1, \dots$, the FDTD propagation scheme is

$$\begin{aligned} E_x^{n+1/2}(x, y) &= E_x^{n-1/2}(x, y) + \frac{\tau}{\epsilon_{\text{eff}}(x, y)} \left[\frac{\partial H_z^n}{\partial y} - J_x^n \right], \\ E_y^{n+1/2}(x, y) &= E_y^{n-1/2}(x, y) - \frac{\tau}{\epsilon_{\text{eff}}(x, y)} \left[\frac{\partial H_z^n}{\partial x} - J_y^n \right], \\ H_z^{n+1}(x, y) &= H_z^n(x, y) + \frac{\tau}{\mu_o} \left[\frac{\partial E_y^{n+1/2}}{\partial x} - \frac{\partial E_x^{n+1/2}}{\partial y} \right] \end{aligned} \quad (2.3a)$$

along with the current-density updates³⁰

$$\begin{aligned} J_x^{n+1}(x, y) &= \left[\frac{1 + \alpha(x, y)\tau/2}{1 - \alpha(x, y)\tau/2} \right] J_x^n(x, y) \\ &\quad + \left[\frac{\beta(x, y)\tau}{1 - \alpha(x, y)\tau/2} \right] E_x^{n+1/2}(x, y), \\ J_y^{n+1}(x, y) &= \left[\frac{1 + \alpha(x, y)\tau/2}{1 - \alpha(x, y)\tau/2} \right] J_y^n(x, y) \\ &\quad + \left[\frac{\beta(x, y)\tau}{1 - \alpha(x, y)\tau/2} \right] E_y^{n+1/2}(x, y). \end{aligned} \quad (2.3b)$$

In addition to the time leapfrogging in Eq. (2.3), we follow the standard FDTD approach of employing evenly spaced but staggered spatial grids,^{4,5} i.e., the x and y grids for E_x , E_y , and H_z are all slightly different, which leads to a particularly accurate evaluation of the relevant derivatives via simple two-point finite differences.

Absorption of field components approaching the boundaries of the grid must be carried out in order to prevent spurious reflections. For each of the x and y grids, absorbing regions are set up in the initial and final portions of these grids and simple exponential damping of the electric and magnetic fields, as typically accomplished in quantum wave-packet work,^{32,33} is carried out after each time step. For example, if x_{\min} and x_{\max} denote the lower and upper values of x , we define left and right absorption strips in $[x_{\min}, x_L]$ and $[x_R, x_{\max}]$. Each field component is then multiplied by $\exp[-s(x-x_L)^2]$ for $x < x_L$ and $\exp[-s(x-x_R)^2]$ for $x > x_R$ (for all y). A similar absorption along the y absorption regions (for all x) is also carried out. Typically, 20%–30% of our grids are devoted to absorption and a gentle strength s , such that, after each absorption, the field values are decreased by 0.9 at the grid edges. (The time steps τ are typically very small, which is why such a gentle absorption is effective.) A better absorption, also with the use of smaller absorbing boundaries, could probably be accomplished with the use of more sophisticated perfectly matched layer approaches.^{5,34}

We employ two types of initial conditions. The simplest one is to specify at $t=0$ some specific pulse. For example, a Gaussian-damped sinusoidal pulse moving from left to right in x with wave vector $k_o = \omega_o/c$ is given by $E_x^{n=-1/2} = 0$ and

$$\begin{aligned} E_y^{n=-1/2}(x, y) &= g_x(x) g_y(y) \cos(k_o x - \omega_o \tau/2), \\ H_z^{n=0}(x, y) &= g_x(x) g_y(y) \cos(k_o x). \end{aligned} \quad (2.4)$$

The Gaussian functions g_x and g_y are then chosen such that the pulse has some desired central position and spatial extent. Owing to the finite extent, the pulse provides frequency content for a range of frequencies about ω_o . Such initial conditions are well suited to computational experiments that probe directly the application of short pulses of light to arbitrary places in MNP array structures. Another type of initial condition we use is a plane-wave source located on a line in y for a fixed value of x . Typically, for some finite time period a plane wave moving forward in x emanates from such a line, with a fixed x value typically chosen to be just after the absorbing boundary in x . Since the wave emanates from a line, it is possible to achieve, effectively, a longer wave train and hence better frequency resolution (if that is desired) than defining a full, long initial pulse on a given grid as above. We find that the scattered field/total field approach for achieving such a source (see, e.g., Ref. 5, and references therein) is reliable and easy to implement. This approach is also somewhat more efficient for obtaining accurate frequency-domain results such as cross sections.

B. Cross-section formulas

We use a simple, direct procedure, which is both feasible and sufficiently accurate for our purposes, to estimate cross

sections (Near- to far-field transformations^{5,6} could provide greater efficiency but we had no need to implement them in this study.) Given real-valued time-dependent electric- and magnetic-field vectors $\mathbf{E}(t) \equiv \mathbf{E}(x, y, z, t)$ and $\mathbf{H}(t) \equiv \mathbf{H}(x, y, z, t)$, as determined in Sec. II A, consistent with an appropriate initial pulse or a source, and scattering off one or more particles, the complex, frequency-resolved total fields are

$$\begin{aligned}\mathbf{E}(\omega) &= \int_0^\infty dt \exp(i\omega t) \mathbf{E}(t), \\ \mathbf{H}(\omega) &= \int_0^\infty dt \exp(i\omega t) \mathbf{H}(t).\end{aligned}\quad (2.5)$$

A comparable calculation, but in the absence of particles, yields incident time-dependent fields $\mathbf{E}_{\text{inc}}(t)$ and $\mathbf{H}_{\text{inc}}(t)$, with the frequency-resolved incident fields

$$\begin{aligned}\mathbf{E}_{\text{inc}}(\omega) &= \int_0^\infty dt \exp(i\omega t) \mathbf{E}_{\text{inc}}(t), \\ \mathbf{H}_{\text{inc}}(\omega) &= \int_0^\infty dt \exp(i\omega t) \mathbf{H}_{\text{inc}}(t).\end{aligned}\quad (2.6)$$

(Analytical results could of course be used for the incident fields. However, a separate numerical calculation of the incident fields with the same grids and other features as for the total fields is more consistent, and will yield more accurate cross sections.) The scattered fields are then given by

$$\mathbf{E}_{\text{sca}}(\omega) = \mathbf{E}(\omega) - \mathbf{E}_{\text{inc}}(\omega), \quad \mathbf{H}_{\text{sca}}(\omega) = \mathbf{H}(\omega) - \mathbf{H}_{\text{inc}}(\omega).\quad (2.7)$$

Following Bohren and Huffman,¹ “cross sections” per unit length of the cylinder axis, which therefore have units of length as opposed to length,² are calculated. The corresponding scattering cross section is

$$\sigma_{\text{sca}}(\omega) = \frac{P_{\text{sca}}(\omega)}{I_{\text{inc}}(\omega)},\quad (2.8)$$

where P_{sca} is the scattered power per unit length (energy/time/length) and I_{inc} is the magnitude of the incident flux or power per unit area. In terms of the (time-averaged) Poynting vector associated with the scattered fields, \mathbf{S}_{sca} , and employing cylindrical coordinates (r, φ, z) ,

$$P_{\text{sca}}(\omega) = r_\infty \int_0^{2\pi} d\varphi \mathbf{S}_{\text{sca}}(\omega) \cdot \mathbf{r}|_{r=r_\infty},\quad (2.9)$$

where the path of integration is along a circle of large radius r_∞ surrounding the cylinder for any value of z , and

$$\mathbf{S}_{\text{sca}}(\omega) = \frac{1}{2} \text{Re}[\mathbf{E}_{\text{sca}}(\omega) \times \mathbf{H}_{\text{sca}}(\omega)^*].\quad (2.10)$$

The absorption cross section is given by

$$\sigma_{\text{abs}}(\omega) = \frac{P_{\text{abs}}(\omega)}{I_{\text{inc}}(\omega)},\quad (2.11)$$

with

$$\begin{aligned}P_{\text{abs}}(\omega) &= r_\infty \int_0^{2\pi} d\varphi \mathbf{S}(\omega) \cdot \mathbf{r}|_{r=r_\infty}, \\ \mathbf{S}(\omega) &= \frac{1}{2} \text{Re}[\mathbf{E}(\omega) \times \mathbf{H}(\omega)^*].\end{aligned}\quad (2.12)$$

The extinction cross section is the sum of the scattering and absorption cross sections,

$$\sigma_{\text{ext}}(\omega) = \sigma_{\text{sca}}(\omega) + \sigma_{\text{abs}}(\omega).\quad (2.13)$$

A useful check of the numerical calculations is to determine the extinction cross section directly via the formula

$$\sigma_{\text{ext}}(\omega) = \frac{P_{\text{ext}}(\omega)}{I_{\text{inc}}(\omega)},\quad (2.14)$$

where

$$\begin{aligned}P_{\text{ext}}(\omega) &= r_\infty \int_0^{2\pi} d\varphi \mathbf{S}_{\text{ext}}(\omega) \cdot \mathbf{r}|_{r=r_\infty}, \\ \mathbf{S}_{\text{ext}}(\omega) &= \frac{1}{2} \text{Re}[\mathbf{E}_{\text{inc}}(\omega) \times \mathbf{H}_{\text{sca}}(\omega)^* + \mathbf{E}_{\text{sca}}(\omega) \times \mathbf{H}_{\text{inc}}(\omega)^*].\end{aligned}\quad (2.15)$$

C. Numerical details

The two-dimensional nature of the problem allows us to employ large, dense grids without excessive computational burden. We generally consider grids in x and y ranging from -1000 to 1000 nm, with the silver cylinder structures centered about the origin. Absorption, as discussed in Sec. II A, is carried out in the first and last 400 nm of each grid, allowing for a 1200×1200 nm interaction region. For cylinders with radii $a = 25$ nm, even a coarse spatial grid spacings $\Delta x = \Delta y = \Delta = 2.7$ nm (750 grid points in each direction) yield reasonable results, although to assure good convergence we have actually used $\Delta = 1$ nm (2000 grid points in each direction) in all the results presented here. Given the current updated equations,³⁰ time steps τ just under the Courant stability limit $\tau_C = \Delta / (3^{1/2} c)$ yield stable solutions; however, for good convergence we chose to use steps $\tau = \tau_C / 2$. A given propagation is generally carried out up to times on the order of 0.15×10^{-13} s, which with our most dense (2000×2000) grid can require several hours of computation time on a 1-GHz Pentium III processor. (However, calculations based on smaller grids of, say, 500×500 dimensions, can be qualitatively correct and require 10–20 min of computer time.)

In estimating cross sections, we Fourier transform on field components along a circle about the origin with $r_\infty = 580$ nm. (Interestingly, almost identical results are obtained with radii as small as $r_\infty = 500$ nm.) A typical source initial condition would correspond to a frequency ω_o in the central portion of the wavelength region of interest, with the source placed just at the edge of the absorption region (e.g., $x = -600$ nm) and turned on for the first 0.65×10^{-15} s.

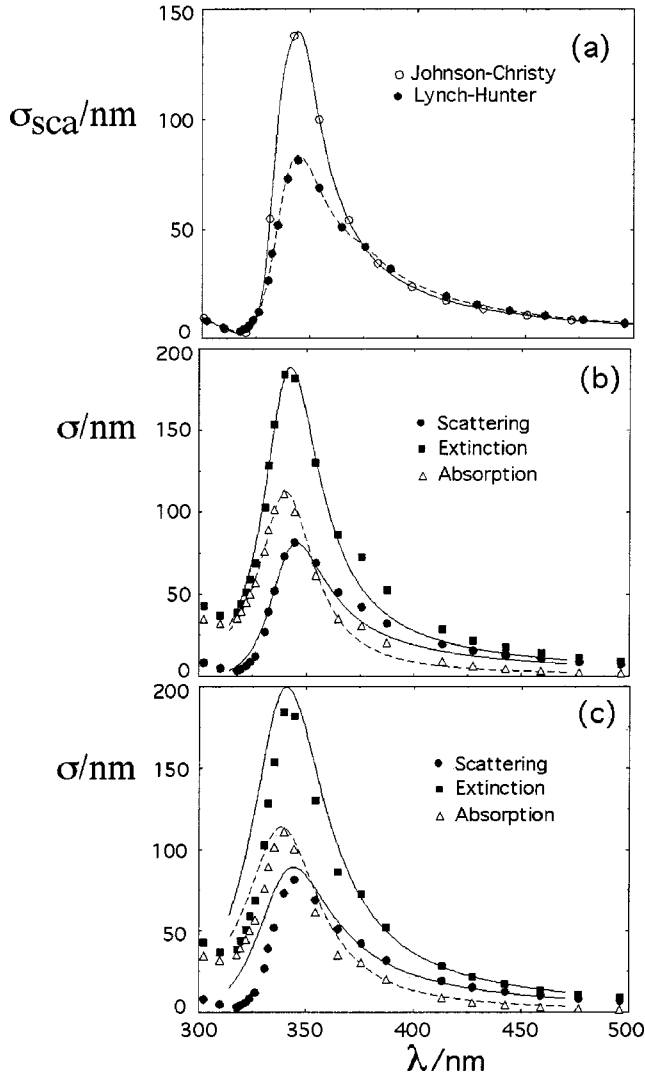


FIG. 1. Cross sections for a single Ag cylinder of radius $a = 25$ nm. (a) Scattering cross sections based on the Johnson-Christy (Ref. 35) (open circles) and Lynch-Hunter (Ref. 36) (filled circles) dielectric constant data. (b) Scattering, absorption, and extinction cross sections calculated with Drude fit D1 of Table I (smooth curves). (c) Cross sections calculated with Drude fit D2 of Table I (smooth curves). In (b) and (c) the symbols represent the cross sections calculated with the explicit dielectric constant data from Lynch and Hunter (Ref. 36).

III. SCATTERING, ABSORPTION, AND EXTINCTION CROSS SECTIONS

A. Isolated cylinders

We first discuss TE scattering off a single Ag cylinder. The analytical solution for this case is known and can be found in, for example, Ref. 1. In addition to establishing key features of the isolated cylinder surface-plasmon resonance, we will also be able to gauge the accuracy of our FDTD calculations.

Figure 1(a) presents the scattering cross section as a function of incident light wavelength for an Ag cylinder of radius $a = 25$ nm. Here we are displaying analytical (*not* FDTD) results for two different sets of empirically inferred Ag di-

TABLE I. Drude parametrizations based on the Lynch-Hunter (Ref. 36) refractive index compilation for silver.

Set	$\epsilon_D(\infty)$	ω_D (eV)	Γ_D (eV)
D1	8.926	11.585	0.203
D2	5.976	9.812	0.259

electric constant data. The open circles are cross sections inferred from the commonly used Johnson and Christy refractive index data set,³⁵ and the filled circles are cross sections inferred from a somewhat more recent compilation of experimental results by Lynch and Hunter.³⁶ It is interesting to note the sensitivity of the cross sections to the underlying dielectric constant data and this should serve as a cautionary note regarding quantitative prediction. We chose to base our calculations on the data compiled by Lynch and Hunter.³⁶

As discussed in the Appendix, we fit Drude models to the empirically inferred dielectric constant data. Table I presents two such parametrizations of the Lynch and Hunter³⁶ compilation, focusing on data in the $\lambda = (2\pi c/\omega) = 300$ –500 nm regime, which we denote as D1 and D2. Figures 1(b) and 1(c) depict the respective cross sections for a 25 nm-radius Ag cylinder as solid or dashed curves. In addition to scattering cross sections, we also display absorption and extinction cross sections. As in Fig. 1(a) the symbols are the cross sections inferred with the empirical dielectric constant data at various wavelengths. Both Drude parametrizations give similar results, although it is clear that set D1 describes the lower wavelength region a bit better than does set D2, and set D2 describes the longer-wavelength regime better. All subsequent results presented are based on the D1 parametrization, although we have verified that the same qualitative features occur with the D2 parametrization.

Figure 2 displays as curves the analytical cross sections for TE scattering off an Ag cylinder with radius $a = 25$ nm obtained with Drude parametrization D1 of Table I, i.e., the same result as that in Fig. 2(b). The symbols in the figure, however, are now the FDTD cross sections estimated from a

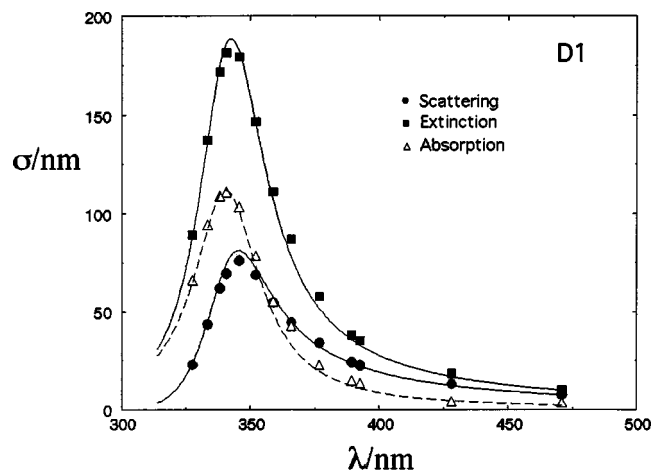


FIG. 2. Comparison of analytical (smooth curves) and FDTD-based (symbols) cross sections for a single Ag cylinder of radius $a = 25$ nm.

single propagation as discussed in Sec. II C, using the same D1 dielectric constant model. The analytical and FDTD cross sections agree to within 10% or better. While the FDTD method has been previously used for the calculation of optical scattering cross sections of various particles (e.g., ice crystals in Ref. 6), we believe this is a demonstration that the FDTD method can reproduce detailed, metal nanoparticle (actually nanowire) scattering cross sections with reasonable accuracy. It must be noted that the fields can become quite large and undergo abrupt changes in the vicinity of the MNP surfaces. The fields also become quite large between MNP's if they are sufficiently close to one another. This makes convergence of cross sections beyond, say, the 5% level difficult to achieve with the present, simple methods.

The large peaks in Fig. 2 are due to the surface plasmon polariton (SPP) resonance.⁷ (The word “polariton,” which is added to signify optically excited surface plasmons, is omitted in some references, e.g., Ref. 1.) We also verified that the FDTD procedure can adequately reproduce the trends in the cross sections with particle size in good agreement with analytical results. For example, as the cylinder radius a increases, the resonance peak redshifts and broadens, and scattering becomes more dominant than absorption. For radius $a=15$ nm, for example, the resonance occurs at $\lambda \approx 340$ nm and near this wavelength $\sigma_{\text{sca}}/\sigma_{\text{abs}} \approx 0.3$, i.e., absorption is more intense than scattering. By $a=100$ nm the resonance has redshifted to $\lambda \approx 350$ nm with scattering, becoming more important than absorption, $\sigma_{\text{sca}}/\sigma_{\text{abs}} \approx 2.3$. The full width at half maximum of, for example, σ_{ext} , expressed in terms of photon energies as opposed to wavelengths, increases from 0.25 at $a=15$ to 1.1 eV at $a=100$ nm. The intensities of all cross sections increase in an approximate linear fashion from $a=15$ to 100 nm, with of course σ_{sca} increasing at a larger rate than σ_{abs} . For example, σ_{sca} increases from 18 to 574 nm between $a=15$ and 100 nm, but σ_{abs} increases from 68 to 247 nm over the same a range. For relatively small radii ($a < 30$ nm) the resonance is mostly dipolar in character. As the radius increases to $a=50$ nm, the dipolar distribution is displaced by a quadrupolar distribution. These features can be verified by plots of the charge density at various times. (Section III B presents explicit results for the charge density of a linear array of cylinders.)

B. Linear arrays of Ag cylinders

Figure 3(a) presents cross sections for two cylinders centered at $(x,y) = (0, -27.5 \text{ nm})$ and $(0, +27.5 \text{ nm})$, each with radius $a=25$ nm. There is thus just a 5-nm space between the two cylinders along y , and the ratio of the distance d between their centers and the cylinder radius is $d/a=2.2$. This configuration is similar to one studied by Kottmann and Martin¹⁷ and our results, although based on a slightly different dielectric constant model, are similar to their results. The cylinders were exposed to y -polarized light moving from left to right along x . This choice of polarization, given the configuration of the particles, is ideally suited to exciting coupled surface-plasmon resonances consistent with induced (and oscillating) dipoles in each cylinder along the y axis. In particular, in the 300–500-nm wavelength region we find

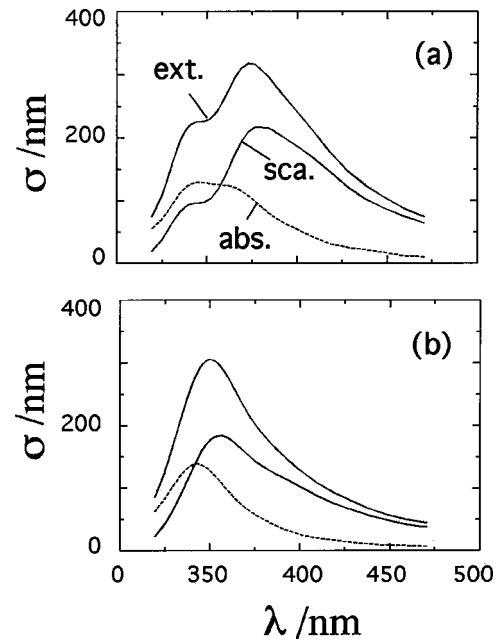


FIG. 3. Cross sections for two $a=25$ -nm Ag cylinders. (a) $d/a=2.2$ and (b) $d/a=3$.

two structures in the cross sections, one a shoulder or weak maximum ($\lambda=340$ nm) close to the single-particle surface-plasmon resonance of Fig. 2, and another, stronger maximum redshifted ($\lambda=375$ nm) from the weaker peak. The presence of extra resonance features relative to the single-particle case is due to the interaction of the cylinders at very short separations. Comparable two-cylinder calculations but with $d/a=3$, i.e., now a 25 nm space between the cylinders along y , displayed in Fig. 3(b), exhibit just one peak and are similar in spirit to the single-particle results. The nature of the resonance structures in Fig. 3 is interesting. Whereas one might naively think the 340 nm structure, owing to its position, is the two-cylinder analog of the single-cylinder dipolar resonance, plots (not shown) of the charge density indicate that it is of mixed dipolar and quadrupolar character, whereas the larger peak to the red of the shoulder is a more of a pure dipolar excitation. Jensen *et al.* have come to similar conclusions in their theoretical studies of a variety of other MNP structures and clusters by examining the polarization vector.²³

Results for $a=25$ nm and four Ag cylinders are given in Fig. 4 for both $d/a=2.2$ [Fig. 4(a)] and $d/a=3$ [Fig. 4(b)]. There is a continuation of the pattern for two cylinders in Fig. 3. For $d/a=2.2$ there are two peaks in the 300–500 nm region, with now the smaller peak near 340 nm being better defined and the larger peak being more redshifted from the smaller peak than the corresponding two-cylinder result. The width of the larger peak is also larger than the two-cylinder result. As with the two-cylinder result, the $d/a=3$ cross sections are simpler and more like the single-particle results, although both the magnitude and widths of the corresponding structures are larger than the single-particle results. It is instructive to examine time snapshots of the charge density, $\rho \propto \nabla \cdot \mathbf{E}$, as done in Ref. 17 for two-cylinder scattering. We have estimated ρ based on carrying out some additional cal-

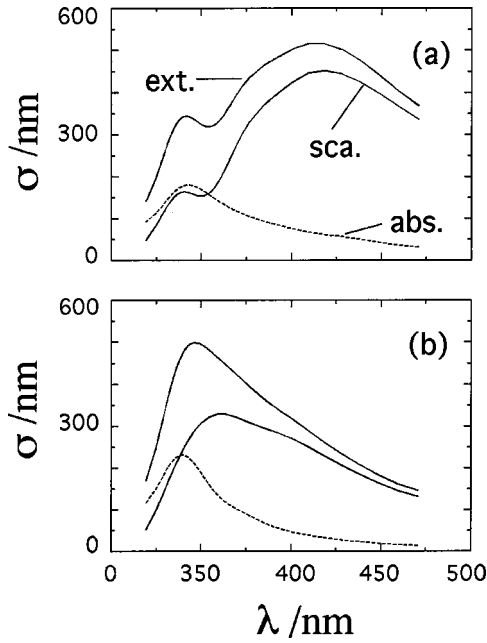


FIG. 4. Cross sections for four $a=25$ -nm Ag cylinders. (a) $d/a=2.2$ and (b) $d/a=3$.

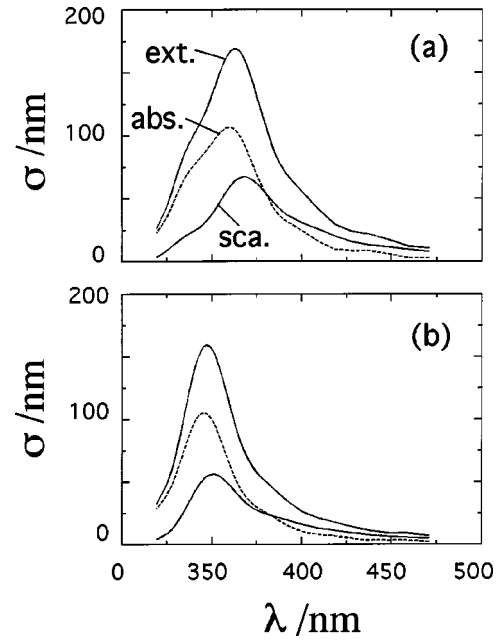


FIG. 6. Cross sections for two $a=15$ nm Ag cylinders. (a) $d/a=2.2$ and (b) $d/a=3$.

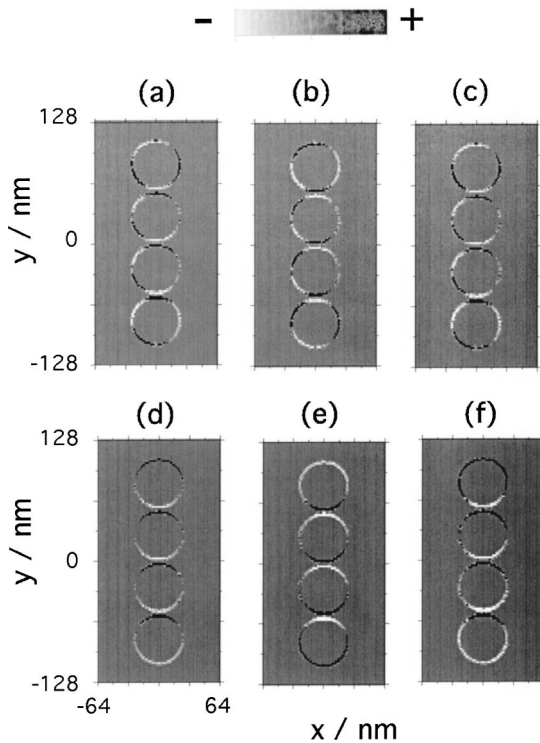


FIG. 5. The instantaneous charge density $\rho(x,y,t)$ for four $a=25$ nm, $d/a=2.2$ Ag cylinders. (a)–(c) Results when illuminated with $\lambda_1=340$ nm light for $t=T-\tau_2/2$, T , and $T+\tau_2/2$, respectively, T being a sufficiently long time after the system has first been illuminated. (d)–(f) Results when illuminated with $\lambda_2=412$ nm light for $t=T-\tau_2/2$, T , and $T+\tau_2/2$.

culations, and using simple finite differences. Figures 5(a)–5(c) result from a propagation in which the four cylinders, with $d/a=2.2$, are exposed to a continuous-wave source with wavelength $\lambda_1=340$ nm, as opposed to the finite duration pulses or sources we used to obtain cross sections over a broad range of wavelengths. The times depicted in Figs. 5(a)–5(c) correspond to approximately $t=T-\tau_1/2$, T , and $T+\tau_1/2$, where $\tau_1=\lambda_1/c$, and T is some time such that the particles have been exposed to several wavelengths of light. Quadrupolar charge structures, oscillating in sign every $\tau_1/2$ time units, are evident. In contrast, when we carry out a similar calculation but with a continuous source of wavelength $\lambda_2=412$ nm, corresponding to the larger, broader peak of Fig. 4(a) we obtain Figs. 5(d)–5(f) for times $t=T-\tau_2/2$, T , and $T+\tau_2/2$, indicative of a dipolar oscillation.

We also studied the two-cylinder case but with a smaller radius, $a=15$ nm. Results very similar to those above for $a=25$ nm were obtained. Figure 6 shows two-cylinder results for $d/a=2.2$ and 3. These results, as well as other results we have obtained for larger arrays, are similar to the $a=25$ nm results such as those in Fig. 3. The main differences are that (i) cross section magnitudes tend to be smaller and (ii) absorption, in the wavelength region on which we are focusing, tends to be more important than scattering. (Note that particle size effects and possibly even quantum effects should be considered in the dielectric constant modeling when considering cylinders with much smaller radii.¹⁹)

We also examined linear arrays of six and eight cylinders, and apart from an increase in all the cross section magnitudes, the results are similar in spirit to those for four cylinders. Throughout this subsection we have focused on light polarized along the linear axis containing all the cylinders. We also considered light polarized normal to this axis. Gen-

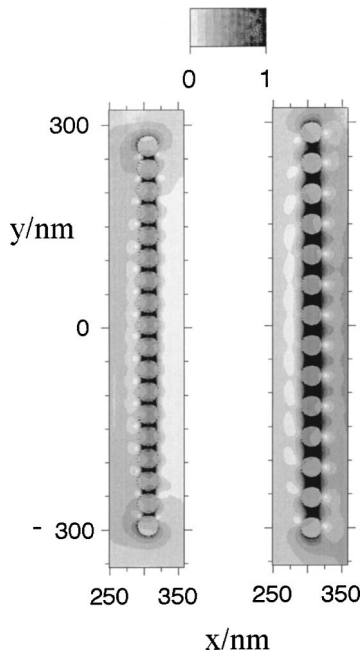


FIG. 7. Magnitude of the electric-field vector at an instant of time after a linear array has interacted with a pulse of y -polarized light moving from left to right. The left panel corresponds to $d/a = 2.2$ and the right panel to $d/a = 3$, with $a = 15$ nm. (In this figure and in all subsequent image figures the same ten image levels are employed, with ranges 0–0.1, 0.1–0.2, ..., 0.8–0.9, 0.9, and higher, in units of the maximum possible field magnitude in the absence of cylinders.)

erally there are weaker interactions in this case (even for $d/a = 2.2$) and the results are similar to those for a single cylinder.

IV. TIME-DOMAIN BEHAVIOR OF LIGHT IN VARIOUS ARRAYS

A. Broad illumination of linear arrays

Linear arrays of cylinders under conditions of broad illumination are most directly related to the cross sections discussed in Sec. III and so we examine these first. We consider arrays exposed to a y -polarized pulse, of x - y dimensions 600×1200 nm, moving from left to right along x , and also arrays exposed to a corresponding continuous wave source. The left panel of Fig. 7 displays typical results for the magnitude of the electric-field vector for an 18-cylinder array with $d/a = 2.2$, $a = 15$ nm, and the right panel displays results for a 14-cylinder array with $d/a = 3$, $a = 15$ nm. In each of these calculations the initial pulse condition with a wavelength $\lambda_0 = 448$ nm is used, and a time instant corresponding to a maximum in the intensity is displayed. The dark spots between the cylinders indicate very intense fields. Although a little unclear from the coarse image scale employed, the peak field magnitudes of the $d/a = 2.2$ case (left) can be more than twice as high as those for the $d/a = 3$ case. Relative to corresponding calculations without the cylinders present, the field intensities ($E_x^2 + E_y^2$) between the cylinders and near their surfaces can be 40 times larger for $d/a = 2.2$ and 9

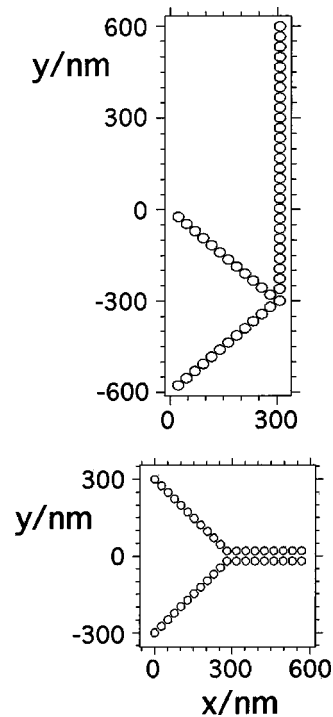


FIG. 8. The upper diagram shows a funnel of cylinders feeding into a linear array of cylinders and the lower diagram shows a funnel feeding into a double chain array along the x axis. Actual dimensions indicated are for radius $a = 15$ nm cylinders. The individual arms and chains have $d/a = 2.2$ in the upper figure and 2.4 in the lower panel. The perpendicular distance between upper and lower cylinder centers in the two parallel chains is 40 nm.

times larger for $d/a = 3$. The corresponding continuous source results (not shown) are qualitatively similar but now the fields can be even larger. Relative to comparable no-cylinder calculations, the $d/a = 2.2$ case is over 100 times more intense and the $d/a = 3$ case is over 25 times larger. Actually, much larger intensities would probably result if we optimized the initial wavelength to be closer to a resonance, as found in Ref. 15 in a more thorough discussion of the two-cylinder case.

B. Funneling light to arrays

The broad illumination calculations of Fig. 7 reveal nothing about propagation of energy up an array. One way to probe for energy transport is to devise some excitation of the lowest cylinder and watch the subsequent flow of intensity. While one can always devise hypothetical single-particle (or cylinder) excitations and propagate them in the presence of an array, the experimental realization of such a scenario is hard to achieve. Our approach, which has the advantage of being experimentally feasible, is to devise a V-shaped configuration of cylinders, as shown (rotated 90°) in Fig. 8, that funnels energy to the region of the point of the V, where one or more arrays are placed to receive and possibly transport the energy. Stockman, Faleev, and Bergman^{20,21} previously explored the possibility of localizing electromagnetic energy in simple V-shaped structures and the configurations studied here represent a generalization of this idea. In what follows

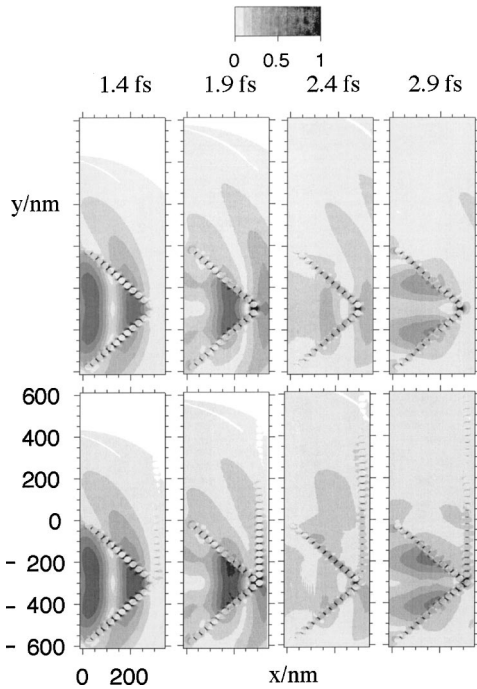


FIG. 9. Time sequence of the magnitude of the electric field as a light pulse interacts with a funnel (upper four panels) and a funnel with a linear array at its mouth (lower four panels). See the upper panel of Fig. 8 for the cylinder configuration, and the caption of Fig. 7 for image level details.

we refer to the V-shape configuration alone as the funnel, and the region at which the point of the V would be as the funnel mouth.

Figure 9 displays time sequences of the magnitude of the electric field corresponding to a 500×500 nm pulse of y -polarized light with $\lambda_o = 448$ nm, moving from left to right. The upper sequence corresponds to light hitting a configuration with just the funnel, and the lower sequence corresponds to the same situation but with a linear array of $d/a = 2.2$, $a = 15$ nm cylinders extending up from the funnel mouth, as in the top panel of Fig. 8. Several things can be noted. First, it is clear from the darkness that develops near the mouth of the funnel in both cases that light is much more intense at the mouth of the funnel. It is also clear, particularly from the final two panels of the lower sequence, that intense light can develop between the cylinders in the linear array. However, it would be incorrect to assert that this “lighting up” of the linear array is due to propagation up the linear array. Rather, it is due to the buildup of low intensity levels of light that are diffracted by the funnel before reaching the mouth. We also carried out calculations for which the funnel is composed of much larger radius cylinders so that, effectively, it has no holes in it. The result is that very little radiation goes up the linear array, with just two or three cylinders near the mouth appreciably excited. The result here is not peculiar to the use of a finite pulse, and comparable results are obtained when a continuous-wave source is employed.

This negative result regarding propagation upward through the linear array is perhaps not surprising in view of

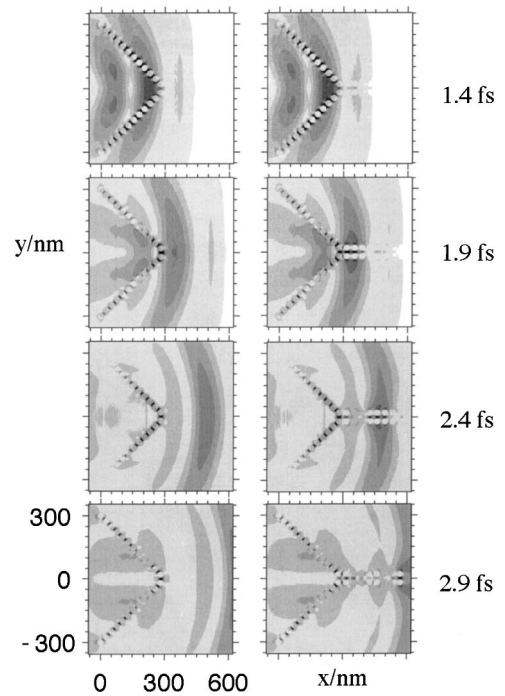


FIG. 10. Time sequence of the magnitude of the electric field as a pulse of light interacts with only the funnel (four panels on left) and a funnel with a double chain at its mouth (four panels on right). See the lower panel of Fig. 8 for the cylinder configuration, and the caption of Fig. 7 for image level details.

several aspects. First, the SPP’s, as our cross section calculations of Sec. III have shown, are rather short lived. The full widths at half maximum of the resonances are greater than 0.25 eV, corresponding to lifetimes on the order of a femto-second or less. It is difficult to set up and maintain a coherent, moving superposition of electromagnetic energy under such conditions. Our result is also consistent with conclusions drawn by Maier, Kik, and Atwater¹⁰ on the basis of FDTD calculations on an array of gold spheres. Furthermore, the action of focusing down the radiation at the funnel mouth leads to a distribution of frequencies. However, we must emphasize that this is just one particular, limited result based on a simple linear array of circular cylinders. A more sophisticated, but promising, alternative to simple linear arrays is discussed below.

We also carried out calculations with the linear array aligned along the x axis, i.e., essentially a Y configuration of cylinders. This led to only small amounts of energy along the linear array. A more promising result, however, came when we considered two parallel chains of cylinders emanating from the cylinder mouth, as outlined in the lower panel of Fig. 8, i.e., a more familiar funnel appearance. Figure 10 displays the result of propagating the same initial condition as used for Fig. 9. Significant light intensity is trapped in a localized region between the two chains near the mouth of the funnel and it clearly is transported down the double chain. The intense fields between the two linear chains are consistent with the broad illumination results above. We have verified that there is definite propagation down the middle in a number of ways, including detailed inspection of movies of the time evolution.

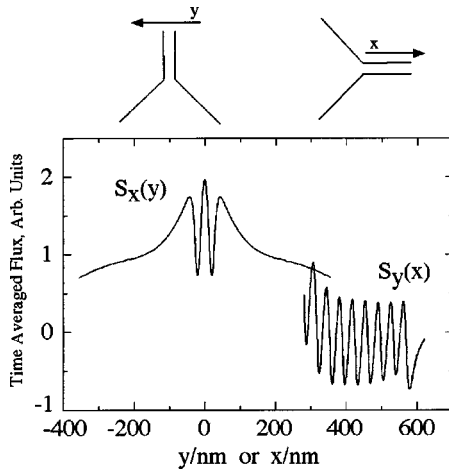


FIG. 11. Time-averaged flux (normal Poynting vector component) across (i) a line along y placed 20 nm in x from the last cylinder centers of the double chain (S_x) and (ii) a line along x placed 20 nm from the top y value of the upper chain cylinder centers (S_y). See also the schematic pictures of the lines at the top of this figure and the lower panel of Fig. 8.

Figure 11 quantifies our result by depicting the time-averaged energy flux crossing a line along y , placed just after the last cylinders in the double chain, as indicated schematically in the top left portion of the figure. (See the figure caption for more details.) The relevant Poynting vector component is $S_x = E_y H_z$. Significant outward (positive) energy flow emanates from a 100 nm region centered over the opening of the double chain. (The distance between the centers of the upper and lower cylinders in the double chain in this case is about 40 nm, and the cylinder radius is 15 nm.) We have verified that the central peak in S_x is more than twice the magnitude of what it would be in the absence of the double chain. The two side peaks, which are close to the cylinder surfaces, as opposed to the region between cylinders, are also large and positive. It is also important to verify that the double chain does not significantly “leak” energy away from its sides. The right side of Fig. 11 shows the flux ($S_y = -E_x H_z$) across a line along x , placed just above the cylinders in the double chain, as schematically indicated in the top right portion of the figure. This flux is clearly significantly lower than the flux emanating from the end of the double chain and, furthermore, fluctuates in sign. The magnitudes of the electric-field intensities also follow the same trends as the Poynting vector components. Of course there is radiation outside the double chain, with the results in Figs. 10 and 11 showing that it is a factor-of-2 (or more) less intense than the radiation near, inside, or emanating from the end of the double chain. From a practical standpoint, it would be better to have intensity enhancements of ten or more, as we saw with the broadly illuminated linear arrays. Also, the propagation is in the direction of the initial light pulse wave vector. Comparable calculations but with a double chain going up the y axis as opposed to along the x axis led to weaker results more akin to those in Fig. 9. Nonetheless we believe our results are encouraging and can probably be significantly improved upon.

The funnel configuration used for Figs. 10 and 11 consisted of cylinders in each chain or funnel arm with $d/a = 2.4$ and $a = 15$ nm, i.e., the cylinders were not quite as close to one another as they were with the $d/a = 2.2$ calculations. (The openings between cylinders are 6-nm wide, as opposed to the rather small 3-nm openings for the $d/a = 2.2$ and $a = 15$ nm calculations.) We chose to use $d/a = 2.4$ because this might be more readily achieved in the laboratory than $d/a = 2.2$. We also carried out similar calculations with $d/a = 2.2$, and they led to very similar results regarding relative intensities. We expect that comparable calculations, but with $d/a = 3$ and larger, will show lower field enhancements within the double chain relative to outside it, owing to increased diffraction. However, there are many variations on this basic funnel configuration that should be investigated, and we wish to defer such further studies to future work.

V. CONCLUDING REMARKS

We presented an FDTD approach to studying the interaction of light with nanoscale radius metallic cylinders or nanowires. We obtained reasonably accurate cross sections for single- and multiple-cylinder arrays, confirming the reliability of our approach. Calculations exploring the explicit time-domain behavior of a variety of arrays were carried out, with the aim of assessing the possibility of nanoscale confinement and propagation of radiation. Our work was motivated by important prior work of several other groups^{8–21} related to such possibilities. We are particularly encouraged by results based on a funnel configuration of cylinders that showed localization and propagation of energy between two parallel chains emanating from the funnel mouth.

There are many directions for future work. It is likely that the intensity of light developing and propagating between the parallel double chains (Fig. 10) can be significantly enhanced by varying the distance between the parallel chains, cylinder radii, relative placements, and of course the wavelength and propagation direction of the incident light. Improved dielectric constant models, valid for a wider frequency range, must also be developed (see the Appendix). Alternatives to circular cylinders should also be considered, e.g., ellipses and triangles,^{18,19} or three-dimensional elongated MNP’s or nanorods.¹⁰ The extension of our approach to arbitrary nanoparticle shapes will also allow us connect more directly with the experimental results of Refs. 12–14.

ACKNOWLEDGMENTS

We received much helpful advice and guidance from Professor G. C. Schatz. The encouragement of our colleagues Drs. G. P. Wiederrecht, G. A. Wurtz, and A. F. Wagner was also invaluable. We were supported by the Office of Basic Energy Sciences, Division of Chemical Sciences, Geosciences, and Biosciences, U.S. Department of Energy, under Contract No. W-31-109-ENG-38.

APPENDIX: DRUDE MODEL FITS TO EMPIRICAL DIELECTRIC CONSTANT DATA FOR SILVER

We first outline the auxiliary differential equations approach⁵ as it applies to the Drude dielectric constant. The resulting time-domain equations have been used numerous times before,^{28,29} but this explicit demonstration of their equivalence to the frequency-domain equations should benefit most readers. We then discuss how we parametrize the Drude model for empirical dielectric constant data for silver.

The frequency-domain Maxwell equation relating $\varepsilon(\omega)\mathbf{E}(\omega) \equiv \varepsilon(x,y,z,\omega)\mathbf{E}(x,y,z,\omega)$ to the curl of $\mathbf{H}(\omega) \equiv \mathbf{H}(x,y,z,\omega)$ is

$$-i\omega\varepsilon(\omega)\mathbf{E}(\omega) = \nabla \times \mathbf{H}(\omega). \quad (\text{A1})$$

Suppose we reexpress $\varepsilon(\omega) = \varepsilon_D(\omega)\varepsilon_o$ as

$$\varepsilon(\omega) = \varepsilon_o\{\varepsilon_D(\infty) + [\varepsilon_D(\omega) - \varepsilon_D(\infty)]\}. \quad (\text{A2})$$

Equation (A1) is then rewritten as

$$\mathbf{J}(\omega) - i\omega\varepsilon_o\varepsilon_D(\infty)\mathbf{E}(\omega) = \nabla \times \mathbf{H}(\omega), \quad (\text{A3})$$

where we identify the current density

$$\mathbf{J}(\omega) = -i\omega\varepsilon_o[\varepsilon_D(\omega) - \varepsilon_D(\infty)]\mathbf{E}(\omega). \quad (\text{A4})$$

The time-domain analog of Eq. (A3) is found by Fourier transforming Eq. (A4) to give

$$\mathbf{J}(t) + \varepsilon_o\varepsilon_D(\infty)\frac{\partial\mathbf{E}(t)}{\partial t} = \nabla \times \mathbf{H}(t), \quad (\text{A5})$$

which is equivalent to the first of Eqs. (2.1). We still need a differential equation to determine $\mathbf{J}(t)$, which is found from Eq. (A4) if an analytical form for $\varepsilon_D(\omega)$ is specified. The Drude model,¹ for example, can be written as

$$\varepsilon_D(\omega) = \varepsilon_D(\infty) - \frac{\omega_D^2}{\omega^2 + i\Gamma_D\omega}. \quad (\text{A6})$$

Insertion of Eqs. (A6) into (A4), followed by Fourier transformation into the time-domain, leads to

$$\frac{\partial^2\mathbf{J}(t)}{\partial t^2} + \Gamma_D\frac{\partial\mathbf{J}(t)}{\partial t} = \omega_D^2\varepsilon_o\frac{\partial\mathbf{E}(t)}{\partial t}, \quad (\text{A7})$$

which can be reduced to

$$\frac{\partial\mathbf{J}(t)}{\partial t} + \Gamma_D\mathbf{J}(t) = \omega_D^2\varepsilon_o\mathbf{E}(t). \quad (\text{A8})$$

Equation (A8) is equivalent to the last of Eqs. (2.1). Eqs. (A5) and (A8), along with the time-domain equation for $\partial\mathbf{H}(t)/\partial t$, allow one to carry out time-domain studies consistent with the complex, frequency-dependent dielectric constant of Eq. (A6).

The Drude model, Eq. (A7), does not provide an accurate model of empirical dielectric constant data for silver over a wide frequency range, particularly if one employs a literal interpretation of the parameters. However, one need not require $\varepsilon_D(\infty)$ to be the true limiting, infinite frequency value for the dielectric constant or ω_D to be the bulk plasmon frequency. If we simply fit the three parameters to empirical data over some given frequency range, a much more flexible and realistic approximation is obtained. We have chosen to focus in the present work on the frequency range consistent with the 300–500-nm wavelength range and have parametrized the Drude model to reasonably describe the corresponding empirical dielectric constant data of Ref. 36 in this range. Actually it is difficult to accurately fit a Drude model to this wide a range of wavelengths. We used a continuous variable simulating annealing technique³⁷ to minimize the sum of squares error associated with the Drude model and the empirical data of Ref. 36 over somewhat narrower wavelength ranges. The D1 parametrization discussed in the text is such a fit of the 325–375-nm empirical data range, whereas the D2 parametrization is a fit over the somewhat broader 325–400-nm range. As discussed, we decided to employ the D1 fit in most of our work. With respect to the 300–500-nm wavelength range of interest, it led to dielectric component errors typically in the 3%–30% range in the middle third of this wavelength region, with somewhat larger errors occurring in the extremes of the full wavelength range. Nonetheless, as shown in the text, the calculated cross sections agree surprisingly well with results based on the correct dielectric constant data.

Alternative analytical forms for the dielectric constant (e.g., Lorentz or Debye) could be used and similar procedures followed. Furthermore, as outlined by Taflove and Hagness,⁵ one can introduce more than one current density ($\mathbf{J}_1, \mathbf{J}_2, \dots$), leading to additional terms in Eq. (A6) and related equations, and achieve additional parameters with a more accurate modeling of empirical data over a wider range. Such an approach will be required for more quantitative modeling.

*Corresponding author. Email address: gray@tcg.anl.gov

¹C. F. Bohren and D. R. Huffman, *Absorption and Scattering of Light by Small Particles*, 2nd ed. (Wiley, New York, 1983).

²E. Betzig and J. K. Trautman, *Science* **257**, 189 (1992).

³C. A. Mirkin, *Science* **286**, 2095 (1999).

⁴K. S. Yee, *IEEE Trans. Antennas Propag.* **14**, 302 (1966).

⁵A. Taflove and S. C. Hagness, *Computational Electrodynamics: The Finite-Difference Time-Domain Method*, 2nd ed. (Artech House, Boston, 2000).

⁶P. Yang and K. N. Liou, *J. Opt. Soc. Am. A* **13**, 2072 (1996).

⁷U. Kreibig and M. Vollmer, *Optical Properties of Metal Clusters*

(Springer, New York, 1995), pp. 52–53.

⁸M. Quinten, A. Leitner, J. R. Krenn, and F. R. Aussenegg, *Opt. Lett.* **23**, 1331 (1998).

⁹S. A. Maier, M. L. Brongersma, P. G. Kik, S. Meltzer, A. A. G. Requicha, and H. A. Atwater, *Adv. Mater. (Weinheim, Ger.)* **13**, 1501 (2001).

¹⁰S. A. Maier, P. G. Kik, and H. A. Atwater, *Appl. Phys. Lett.* **81**, 1714 (2002).

¹¹J. R. Krenn, B. Lamprecht, H. Ditlbacher, G. Schider, M. Lalerno, A. Leiner, and F. R. Aussenegg, *Europhys. Lett.* **60**, 663 (2002).

¹²G. A. Wurtz, N. M. Dimitrijevic, and G. P. Wiederrecht, *Jpn. J.*

- Appl. Phys., Part 2 **41**, L351 (2002).
- ¹³J. Hranisavljevic, N. M. Dimitrijevic, G. A. Wurtz, and G. P. Wiederrecht, *J. Am. Chem. Soc.* **124**, 4536 (2002).
- ¹⁴G. A. Wurtz, J. Hranisavljevic, and G. P. Wiederrecht, *J. Microsc.* **210**, 340 (2003).
- ¹⁵Y.-H. Liao, S. Egusa, and N. F. Scherer, *Opt. Lett.* **27**, 857 (2002).
- ¹⁶M. J. Feldstein, C. D. Keating, Y.-H. Liao, M. J. Natan, and N. F. Scherer, *J. Am. Chem. Soc.* **119**, 6638 (1997).
- ¹⁷J. P. Kottmann and O. J. F. Martin, *Opt. Express* **12**, 655 (2001).
- ¹⁸J. P. Kottmann, O. J. F. Martin, D. R. Smith, and S. Schultz, *Chem. Phys. Lett.* **341**, 1 (2001).
- ¹⁹J. P. Kottmann, O. J. F. Martin, D. R. Smith, and S. Schultz, *Phys. Rev. B* **64**, 235402 (2001).
- ²⁰M. I. Stockman, S. V. Faleev, and D. J. Bergman, *Phys. Rev. Lett.* **88**, 067402 (2002).
- ²¹M. I. Stockman, S. V. Faleev, and D. J. Bergman, *Appl. Phys. B: Lasers Opt.* **74** (Suppl.), S63 (2002).
- ²²G. C. Schatz, *Acc. Chem. Res.* **17**, 370 (1984).
- ²³T. Jensen, L. Kelly, A. Lazarides, and G. C. Schatz, *J. Cluster Sci.* **10**, 295 (1999).
- ²⁴K. L. Kelly, A. A. Lazarides, and G. C. Schatz, *Compt. Sci Eng.* **3**, 67 (2001).
- ²⁵K. L. Kelly, T. R. Jensen, A. A. Lazarides, and G. C. Schatz, in *Metal Nanoparticles: Synthesis, Characterization and Applications*, edited by D. Feldheim and C. Foss (Marcel Dekker, New York, 2001), pp. 89–118.
- ²⁶T. R. Jensen, M. L. Duval, K. L. Kelly, A. A. Lazarides, G. C. Schatz, and R. P. Van Duyne, *J. Phys. Chem. B* **103**, 9846 (1999).
- ²⁷A. A. Lazarides, K. L. Kelly, T. R. Jensen, and G. C. Schatz, *J. Mol. Struct.: THEOCHEM* **529**, 59 (2000).
- ²⁸J. B. Judkins and R. W. Ziolkowski, *J. Opt. Soc. Am. A* **12**, 1974 (1995).
- ²⁹R. W. Ziolkowski and M. Tanaka, *J. Opt. Soc. Am. A* **16**, 930 (1999).
- ³⁰S. A. Cummer, *IEEE Trans. Antennas Propag.* **45**, 392 (1997).
- ³¹J. Vuckovic, M. Loncar, and A. Scherer, *IEEE J. Quantum Electron.* **36**, 1131 (2000).
- ³²R. H. Bisseling, R. Kosloff, and J. Manz, *J. Chem. Phys.* **83**, 993 (1985).
- ³³R. Kosloff and D. Kosloff, *J. Comput. Phys.* **63**, 363 (1986).
- ³⁴J.-P. Berenger, *J. Comput. Phys.* **114**, 185 (1994).
- ³⁵P. B. Johnson and R. W. Christy, *Phys. Rev. B* **6**, 4370 (1972).
- ³⁶D. W. Lynch and W. R. Hunter, in *Handbook of Optical Constants of Solids*, edited by E. D. Palik (Academic, Orlando, 1985), pp. 350–357.
- ³⁷W. H. Press, B. P. Flannery, S. A. Teukolsky, and W. T. Vetterling, *Numerical Recipes in Fortran*, 2nd ed. (Cambridge University, New York, 1992). Note that the first edition of this book does not contain the continuous variable simulated annealing algorithm.